A&A 455, 441–451 (2006)
DOI: 10.1051/0004-6361:20042606

Astronomy & Astrophysics

Weak lensing measurements of dark matter halos of galaxies from COMBO-17

M. Kleinheinrich[1,2], P. Schneider[2], H.-W. Rix[1], T. Erben[2], C. Wolf[3], M. Schirmer[2], K. Meisenheimer[1], A. Borch[1], S. Dye[4], Z. Kovacs[1], and L. Wisotzki[5]

[1] Max-Planck-Institut für Astronomie, Königstuhl 17, 69117 Heidelberg, Germany
e-mail: martina.kleinheinrich@uni-due.de
[2] Institut für Astrophysik und Extraterrestrische Forschung, Universität Bonn, Auf dem Hügel 71, 53121 Bonn, Germany
[3] Department of Physics, Denys Wilkinson Bldg., University of Oxford, Keble Road, Oxford, OX1 3RH, UK
[4] School of Physics and Astronomy, Cardiff University, 5 The Parade, Cardiff, CF24 3YB, UK
[5] Astrophysikalisches Institut Potsdam, An der Sternwarte 16, 14482 Potsdam, Germany

Received 23 December 2004 / Accepted 19 April 2006

ABSTRACT

We present mass estimates for dark matter halos around galaxies from the COMBO-17 survey using weak gravitational lensing. COMBO-17, with photometry in 17 optical filters, provides precise photometric redshifts and spectral classification for objects with $R < 24$. This permits to select and sort lens and source galaxies by their redshifts and lens luminosity or color, which bypasses many uncertainties in other weak lensing analyses arising from broadly estimated source and lens redshifts. We study the shear created by dark matter halos around 12 000 galaxy lenses at redshifts $z_d = 0.2$–0.7 by fitting the mass normalization of either singular isothermal spheres (SIS) or Navarro-Frenk-White (NFW) profiles to background source orientations around the whole lens sample. We also consider halos around blue and red subsamples separately and constrain the scaling of halo mass with light. For the NFW model, we find virial masses $M^*_{\rm vir} = 3.9\times10^{11}h^{-1}\ M_\odot$ for blue and $M^*_{\rm vir} = 7.1\times10^{11}h^{-1}\ M_\odot$ for red galaxies of $L_\star = 10^{10}h^{-2}\ L_\odot$, respectively. The 1-$\sigma$ uncertainty on $\log M^*_{\rm vir}$ for the whole lens sample is about 0.2. We compare our results to those obtained from the Red-Sequence Cluster Survey (RCS) and the Sloan Digital Sky Survey (SDSS). Taking differences in the actual modelling into account, we find very good agreement with these surveys.

Key words. gravitational lensing – galaxies: fundamental parameters – galaxies: statistics – cosmology: dark matter

1. Introduction

Dark matter is the dominant mass component in the universe and also the major constituent of cosmological structures like galaxy clusters or galaxies. Therefore, dark matter plays a fundamental role in the formation and evolution of these structures. Our understanding of structure formation is thus limited by our ability to map the dark matter distribution in these objects. In this paper, we will investigate the dark matter distribution around galaxies.

Several methods have been applied to measure masses of galaxies: rotation curves of spiral galaxies provided the first evidence for dark matter in galaxies (e.g. Sofue & Rubin 2001). In elliptical galaxies, the dynamics of e.g. the stellar population itself, globular clusters or planetary nebulae can be used (e.g. Danziger 1997). However, these methods can only be applied over radii where luminous tracers are available (a few tens of kpc) and suffer from typical problems of dynamical studies, e.g. the unknown degree of anisotropy (Rix et al. 1997).

In a few cases it is possible to measure masses from X-rays or, within the Einstein radius, from strong lensing (e.g. Kochanek et al. 2004).

Only two methods are currently in use to probe dark matter halos of galaxies at scales of about $100h^{-1}$ kpc or larger: weak gravitational lensing and the dynamics of satellite galaxies. At these scales, the baryonic contribution to the mass is negligible, so that basically just the dark matter around galaxies is probed. In the beginning, satellite dynamics was only applied to isolated spiral galaxies (Zaritsky et al. 1993; Zaritsky & White 1994; Zaritsky et al. 1997). Later, early-type galaxies were investigated (McKay et al. 2002; Prada et al. 2003; Brainerd & Specian 2003; Conroy et al. 2005), and now galaxies in denser environments and at much fainter magnitudes are also studied (van den Bosch et al. 2004). Weak gravitational lensing has become a standard tool in recent years. Its main advantage over satellite dynamics it that no assumptions on the dynamical state of the galaxies under consideration have to be made.

Galaxy-galaxy lensing is the technique which uses the image distortions of background galaxies to study the mass distribution in foreground galaxies. Galaxy-galaxy lensing and satellite dynamics are independent methods and it is very desirable to have both methods available for comparison of results. Weak gravitational lensing is similar to the use of satellite dynamics in the sense that only statistical investigations are possible due to the weakness of the gravitational shear and the small number of satellites per primary galaxy. The most recent results from both techniques are summarized in Brainerd (2004).

Galaxy-galaxy lensing was measured for the first time by Brainerd et al. (1996). In early work, people concentrated on isothermal models for describing the lenses (Brainerd et al. 1996; Griffiths et al. 1996; dell'Antonio & Tyson 1996; Hudson et al. 1998; Fischer et al. 2000; Smith et al. 2001; Wilson et al. 2001; Hoekstra et al. 2003). The best-constrained parameter was the effective halo velocity dispersion for $\sim L_\star$ galaxies, assuming a scaling relation between the velocity dispersion and the

luminosity according to the Tully-Fisher and Faber-Jackson relations. The Tully-Fisher index η in this relation (see Sect. 4) was typically assumed according to measurements from the central parts of the galaxies. Only Hudson et al. (1998) were able to put at least a lower limit on η. More generally, the galaxy-mass correlation function was later investigated (McKay et al. 2001; Sheldon et al. 2004) and the Navarro-Frenk-White (NFW) profile was considered (Seljak 2002; Guzik & Seljak 2002; Hoekstra et al. 2004). The Sloan Digital Sky Survey (SDSS) has turned out to be extremely powerful for galaxy-galaxy lensing studies (Fischer et al. 2000; McKay et al. 2001; Seljak 2002; Guzik & Seljak 2002; Sheldon et al. 2004; Seljak et al. 2005). Most of its success is due to the fact that the SDSS provides a large sample of lens galaxies with measured spectra. The spectra provide very accurate redshifts and classification of the lens galaxies. Therefore, it is possible to measure dark matter halos as function of luminosity, spectral type or environment of the galaxies. However, the SDSS is a very shallow survey and is thus only able to measure lens galaxies around $z_{\rm d} \approx 0.1$. The question of halo properties at higher redshift and of evolution cannot be addressed. Therefore, substantial effort goes into measurements of galaxy-galaxy lensing at higher redshift with at least rough redshift estimates for the lenses from e.g. photometric redshifts. Currently available are the Hubble Deep Fields which are far too small to provide statistically clean samples free from cosmic variance. Wilson et al. (2001) addressed the question of evolution, but only for early-type galaxies. Hoekstra et al. (2003) had redshifts available for part of their lenses, but not yet enough to split the lenses into subsamples and to study their properties separately. Hoekstra et al. (2004) use the larger Red-Sequence Cluster Survey (RCS) with deep observations. No redshift or color information is available, yet, so that again only properties averaged over all classes of galaxies can be investigated.

Here, we will use the COMBO-17 survey which is a deep survey, that provides accurate photometric redshifts and spectral classification from observations in a total of 17 filters (Wolf et al. 2001, 2003, 2004). This data set allows us to probe lens galaxies at higher redshift ($z_{\rm d} = 0.2{-}0.7$), to derive the relation between luminosity and velocity dispersion (or mass) instead of assuming it and to measure dark matter halos for blue and red galaxies separately. In addition to the singular isothermal sphere (SIS) we will also apply the NFW profile (Navarro et al. 1995, 1996, 1997).

This paper is organized as follows: in Sect. 2 we briefly describe the data set and in Sect. 3 our method of measuring galaxy-galaxy lensing. Section 4 gives our results from the SIS model and Sect. 5 those from the NFW profile. In Sect. 6 we investigate how our measurements are affected by the presence of large foreground clusters in one of the survey fields. In Sect. 7 we will compare our results to those from the RCS and the SDSS. We close with a summary in Sect. 8. Throughout the paper we assume $(\Omega_{\rm m}, \Omega_\Lambda) = (0.3, 0.7)$ and $H_0 = 100h$ km s^{-1} Mpc^{-1}.

2. Data

Our analysis is based on the COMBO-17 survey. COMBO-17, "Classifying Objects by Medium-Band Observations in 17 filters", comprises observations in five broad-band filters ($UBVRI$) and 12 medium-band filters that are used to derive reliable classification and redshift estimates for objects down to $R = 24$. Extensive comparison with spectroscopic redshifts from YVDS (Le Fèvre et al. 2005) has shown that the median precision of the COMBO-17 redshift estimates is $\delta z/(1+z) = 0.02$ (Wolf et al. 2004).

COMBO-17 covers three disjoint fields of $30' \times 30'$ each. Only one of the survey fields is a "random field"; a second is centered on the Chandra Deep Field South, and the third was chosen to study the supercluster system Abell 901a/b, Abell 902 and represents thus an overdense line-of-sight. In Sect. 6 we will investigate the influence of the supercluster system on the galaxy-galaxy lensing measurement. The average of these three fields should not be too far from cosmic average.

The data set used here is exactly the same as in the method-focused companion paper Kleinheinrich et al. (2005). We refer the reader to this paper for details on the COMBO-17 survey and the shape measurements and just summarize the most relevant points. The COMBO-17 (Wolf et al. 2003, 2004) project provided deep R-band imaging ($R \sim 26$, 5σ) at a seeing of ($\sim 0\farcs75$) over three disjoint fields of about 0.26 square degrees each, along with redshift estimates from 17 band photometry, which are accurate to $\sigma_z/(1+z) < 0.01$ (at $R < 21$) and to $\sigma_z/(1+z) \approx 0.05$ at the redshift sample limit of $R \approx 24$. The R-band images, which are the basis of the image shape measurements for the lensing analysis, were augmented with public archival ESO data, and reduced with a pipeline that was optimized for weak lensing (Schirmer et al. 2003). Shapes, expressed by the complex ellipticity χ, were measured with a variant of the KSB algorithm (Kaiser et al. 1995; Luppino & Kaiser 1997; Hoekstra et al. 2000), as implemented by Erben et al. (2001).

2.1. Tangential shear measurement

Before presenting our more rigorous analysis of the COMBO-17 data, exploiting the full reshift and lens luminosity information in the data, we show in Fig. 1 a measurement of the mean tangential shear. This estimator has long been used to present a weak lensing signal (e.g. Brainerd et al. 1996). The shear estimates in the left panel of Fig. 1 were obtained as follows: we selected as lenses all galaxies in the magnitude range $R = 18{-}22$ (Vega) with redshift $z_{\rm d} = 0.2{-}0.7$, as sources all galaxies with $R = 18{-}24$ and $z_{\rm s} = 0.8{-}1.4$ and considered only lens-source pairs with separations $\theta \geq 8''$ (see Sect. 3.1). The tangential shear of a given source, at position $(x_{\rm s}, y_{\rm s})$ and with psf-corrected ellipticity (ϵ_1, ϵ_2), relative to a given lens at position $(x_{\rm d}, y_{\rm d})$ is defined as $\epsilon_t = -[\epsilon_1 \cos(2\alpha) + \epsilon_2 \sin(2\alpha)]$, where $\tan(\alpha) = (y_{\rm s} - y_{\rm d})/(x_{\rm s} - x_{\rm d})$.

We bin the lens-source pairs by their projected separation r at the redshift of the lens and calculate a weighted mean tangential shear $\langle\epsilon_t\rangle$ for all pairs per bin. The weighting takes into account only the noise in the psf-corrected ellipticities ϵ of the sources. The weight of each source is taken as the inverse of the variance $\sigma_\epsilon^2 = \frac{1}{N}\sum|\epsilon^2|$ of the $N = 20$ objects being closest to the source in θ_h – S/N space. Here, θ_h is the half-light radius and S/N is the signal-to-noise of the source – see Erben et al. (2001) and Kleinheinrich et al. (2005) for details on this weighting scheme. In particular, no weighting according to the luminosity of the lens is applied. The error bars are obtained from repeating this measurement a hundred times with randomized source orientations.

The right panel of Fig. 1 was obtained in the same way as the left panel, but after rotating the sources by 45 degrees. The signal is consistent with zero indicating that the measured tangential shear is indeed due to gravitational lensing.

Note that we do not use the measurement of the mean tangential shear in our actual analysis of the data, as this approach

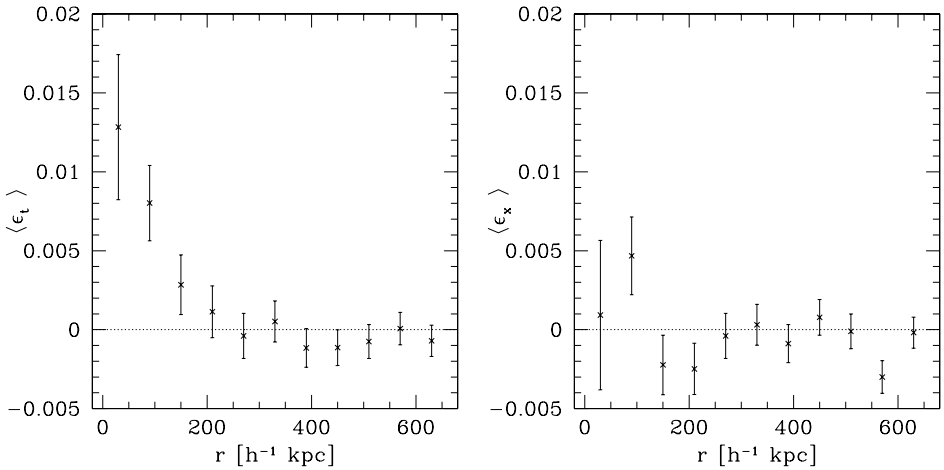

Fig. 1. *Left panel*: averaged tangential shear $\langle\epsilon_t\rangle$ as a function of projected separation between lens and source; *right panel*: same as left panel but sources being rotated by 45 degrees.

does not exploit e.g. the redshift and luminosity information we have for lenses. However, the plots shown in Fig. 1 might be helpful for comparison with results from other data sets.

3. Method

To quantify statistically the shear induced into background images by foreground galaxy halos (the "galaxy-galaxy lensing") we use the maximum-likelihood method proposed by Schneider & Rix (1997). Assuming a specific halo lens model one can compute the shear γ_{ij} on each source j from each lens i. In practise, we use only those lenses whose projected separation r at the redshift of the lens does not exceed a given $r_{\rm max}$. Sources too close to the field boundaries, which might be lensed by galaxies outside the area of the data set, are excluded.

Because the shear from individual galaxies is weak and because several halos may contribute comparably to the shear of a given source position we sum the shear contribution from different lenses to derive the total shear acting on source j:

$$\gamma_j = \sum_i \gamma_{ij}. \tag{1}$$

From the shear and the observed, psf-corrected ellipticity ϵ_j one can estimate the intrinsic ellipticity $\epsilon_j^{(s)}$,

$$\epsilon_j^{(s)} = \epsilon_j - \gamma_j, \tag{2}$$

observed in the absence of lensing. Note that the ellipticity in this notation is a vector in the complex plane that also encodes the position angle of an elongated image. The probability for observing this intrinsic ellipticity is given by

$$P\left(\epsilon_j^{(s)}\right) = \frac{1}{\pi\sigma_\epsilon^2}\exp\left[-\frac{|\epsilon_j^{(s)}|^2}{\sigma_\epsilon^2}\right] \tag{3}$$

where σ_ϵ is the width of the intrinsic ellipticity distribution and the dependence on the absolute value only encodes an isotropic orientation of projected orientation. Multiplying the probabilities from all sources gives the likelihood for a given set of parameters of the lens model. The value of σ_ϵ must be estimated for each source individually, because it depends on its signal-to-noise and half-light radius, see Sect. 2.1 and Kleinheinrich et al. (2005) for details; typical values are $\sigma_\epsilon \approx 0.4$.

In this approach the most likely model is one that produces shear-corrected source orientations that are isotropically oriented.

Note that in this modelling approach the common statistic of shear strength vs. projected radius (shown in Fig. 1) is never used, as we use a S/N-optimized individual shear estimate for each image, which depends on the global lens model.

3.1. Lens and source selection

With the COMBO-17 data set we can select lenses and sources based on their redshifts. We only use objects classified as galaxies or likely galaxies by COMBO-17. Both lenses and sources lie in the magnitude range $R = 18{-}24$ (Vega). The bright limit was set to avoid saturation, while the faint limit is given by the magnitude limit down to which the classification and redshift estimation in COMBO-17 works reliably. Note that with such redshifts we are able to include faint lenses and bright sources.

Our lens sample consists of all galaxies with redshift $z_{\rm d} = 0.2{-}0.7$. Lenses with higher redshifts would not add much to the constraints because only a small number of sources would lie behind them. Lenses at smaller redshifts are excluded because for them a given $r_{\rm max}$ corresponds to a large angular separation θ. Because we exclude all sources for which lenses might lie outside the field boundaries we would therefore have to exclude too many sources.

We chose sources with individual redshift estimates in the redshift range $z_{\rm s} = 0.3{-}1.4$, although in principle we could also include sources for which only statistical redshifts are available. However, in Kleinheinrich et al. (2005) we found that the inclusion of these sources does not improve the constraints, probably because sources that are too faint to get individual redshift estimates also have too noisy shape measurements. A potential lens-source pair is only evaluated if $z_{\rm s} > z_{\rm d} + 0.1$. The minimum redshift difference of $\mathrm{d}z = 0.1$ is chosen to remove pairs where, due to redshift errors, the source is actually in front of the lens or physically close to it. Thus, we minimize the contamination from intrinsic alignments (Heymans & Heavens 2003; King & Schneider 2002).

In the absence of survey image edges and systematic shape measurement errors, there is no a priori need to set a value for $r_{\rm max}$; the large number of images with tiny shear contributions from a given lens galaxy should still add signal to the estimate.

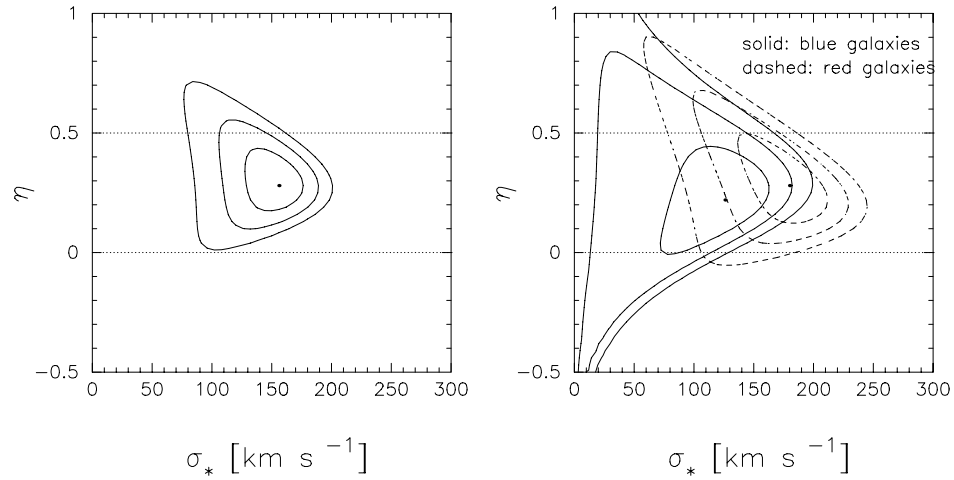

Fig. 2. Constraints on the velocity dispersion $\sigma_\star$ and the Tully-Fisher index η for the SIS model with $r_{\rm max} = 150h^{-1}$ kpc using all lenses (*left panel*) and subsamples of blue and red lenses (*right panel*). Contours are 1-, 2- and 3-σ.

However, in practice a choice of $r_{\rm max}$ is sensible for a variety of reasons. First, a SIS model has a diverging cumulative mass profile that is unphysical. Second, a very large value of $r_{\rm max}$ excludes too many source images from the analysis due to edge effects. Third, at separations of $\geq 500h^{-1}$ kpc our underlying halo model assumption, that halos are spherical, isolated and spatially uncorrelated, breaks down. Therefore, we probe lens galaxy halos out to some projected, physical distance $r_{\rm max}$ from their center. With individual lens redshifts, this can be converted to an angular separation $\theta_{\rm max}$ that can vary among different lens-source pairs. When working with the SIS model (Sect. 4) we use $r_{\rm max} = 150h^{-1}$ kpc, $r_{\rm max} = 250h^{-1}$ kpc and $r_{\rm max} = 400h^{-1}$ kpc. Note that for radii larger than $100h^{-1}$ kpc, there is evidence (e.g. Prada et al. 2003) from satellite dynamics, that a SIS is a poor approximation to the dark matter profile. When modelling the lenses by NFW profiles we use a maximum separation of $r_{\rm max} = 400h^{-1}$ kpc to ensure that the region around the virial radius is probed even for the most massive galaxies.

Shapes can only be measured reliably if objects do not have nearby images. Therefore, we only use lens-source pairs with a minimum angular separation $\theta = 8''$. At $z_{\rm d} = 0.2$ this translates into a physical separation $r = 18.5h^{-1}$ kpc, at $z_{\rm d} = 0.7$ into $r = 40h^{-1}$ kpc.

In addition to fitting halo properties by averaging over all lenses, we will also consider blue and red subsamples based on rest-frame colors. The definitions of "red" and "blue" are based on the "red sequence" of galaxies in the color-luminosity plane, found to be present to $z \sim 1$ in COMBO-17 (Bell et al. 2004). Galaxies with $\langle U - V\rangle \leq 1.15{-}0.31 \times z - 0.08(M_V - 5\ \log\ h + 20)$ define the blue sample while all other galaxies are in the red sample (Bell et al. 2004). In total, our data set contains 11 230 blue and 2580 red lens candidates. The average redshift and SDSS r-band rest-frame luminosities are $\langle z_{\rm d}\rangle = 0.46$ and $\langle L\rangle = 0.41 \times 10^{10}h^{-2}\ L_\odot$ for the blue sample and $\langle z_{\rm d}\rangle = 0.44$ and $\langle L\rangle = 1.27 \times 10^{10}h^{-2}\ L_\odot$ for the red sample, respectively.

4. Results from the SIS model

4.1. Model

The density distribution of the SIS is given by

$$\rho(r) = \frac{\sigma_{\rm v}^2}{2\pi G}\frac{1}{r^2} \tag{4}$$

where $\sigma_{\rm v}$ is the velocity dispersion of a galaxy. Because in our galaxy-galaxy lensing analysis we have to average over lenses with a range of luminosities, we use Faber-Jackson and Tully-Fisher-like relations between the SIS velocity dispersion and luminosity:

$$\frac{\sigma_{\rm v}}{\sigma_*} = \left(\frac{L}{L_*}\right)^\eta, \tag{5}$$

where σ_* is the velocity dispersion of an L_* galaxy. We use $L_* = 10^{10}h^{-2}\ L_\odot$ measured in the SDSS r-band. For the Faber-Jackson and Tully-Fisher relations, which refer to the inner 2−20 kpc, a scaling index of $\eta \approx 1/4$ or $\eta \approx 1/3$ is found.

The (aperture) mass-to-light ratio of the galaxies is determined by η:

$$\frac{M(r \leq R)}{L} = \frac{2\sigma_\star^2 (L/L_\star)^{2\eta} R}{GL} \propto L^{2\eta-1}. \tag{6}$$

So for $\eta = 0.25$ one has $M/L \propto L^{-0.5}$ inside a fixed aperture while $M/L \propto L^0 = $ const. requires $\eta = 0.5$.

For each lens-source pair the shear amplitude is given by

$$\gamma(r) = \frac{2\pi\sigma_{\rm v}^2}{c^2}\frac{D_{\rm ds}}{D_{\rm s}}\frac{1}{\theta}, \tag{7}$$

resulting in an image stretch perpendicular to the projected lens-source direction.

4.2. Results for all galaxies

The left panel of Fig. 2 shows likelihood contours (the product of all terms as in Eq. (3)) when all lenses are used and $r_{\rm max} = 150h^{-1}$ kpc is adopted. The best-fit parameters (with their 68% confidence regions) are $\sigma_\star = 156^{+18}_{-24}$ km s^{-1} and $\eta = 0.28^{+0.12}_{-0.09}$. These estimates for the halo properties agree very well with values for the stellar body from the Tully-Fisher or Faber-Jackson relation, although the radial scale probed here is an order of magnitude larger. The (aperture) mass-to-light ratio scales with luminosity as $M/L \propto L^{-0.44}$. The mass-to-light ratio at fixed radius therefore decreases with increasing luminosity.

We also explored values of $r_{\rm max}$ larger than $150h^{-1}$ kpc. For $r_{\rm max} = 250h^{-1}$ kpc we find $\sigma_\star = 138^{+18}_{-18}$ km s^{-1} and

Table 1. Results for the SIS model for different lens samples and $r_{\rm max} = 150h^{-1}$ kpc. $N_{\rm d}$, $N_{\rm s}$ and $N_{\rm p}$ are the numbers of lenses, sources and pairs in each measurement. Note that the number of sources can vary for different lens selections because not all source candidates are always lying within $r_{\rm max}$ of a lens. The best fit values of σ_* and η are given with 1-σ error bars. The last two columns give the aperture mass within $150h^{-1}$ kpc and the corresponding mass-to-light ratio.

Lenses	$N_{\rm d}$	$N_{\rm s}$	$N_{\rm p}$	$\sigma_\star$ [km s^{-1}]	η	$M_\star$ [$10^{12}h^{-1}\,M_\odot$]	$M_\star/L_\star$
all	12 167	17 640	105 500	156^{+18}_{-24}	$0.28^{+0.12}_{-0.09}$	$1.70^{+0.41}_{-0.48}$	170^{+41}_{-48}
blue	9875	17 335	83 903	126^{+30}_{-36}	$0.22^{+0.15}_{-0.15}$	$1.11^{+0.59}_{-0.54}$	111^{+59}_{-54}
red	2292	11 063	21 597	180^{+24}_{-30}	$0.28^{+0.15}_{-0.12}$	$2.26^{+0.64}_{-0.69}$	226^{+64}_{-69}

$\eta = 0.31^{+0.12}_{-0.12}$ while for $r_{\rm max} = 400h^{-1}$ kpc we find $\sigma_\star = 120^{+18}_{-30}$ km s^{-1} and $\eta = 0.40^{+0.21}_{-0.15}$. There is a clear decrease in $\sigma_\star$ when larger scales of the galaxy halos are probed. Further, we see a systematic increase of η with scale. These trends of $\sigma_\star$ and η with scale show that the model adopted here to describe the lenses is too simple. Several causes are possible: the density profiles of dark matter halos might decline more steeply than r^{-2} as also implied by satellite dynamics (Prada et al. 2003). Alternatively, the environment of the lens galaxies might contribute differently on different scales or the contribution of different subclasses of lenses might change with scale. This all clearly shows that when comparing results from different galaxy-galaxy lensing studies it is important to compare measurements obtained at similar scales.

4.3. Results for blue/red subsamples

For $r_{\rm max} = 150h^{-1}$ kpc, the results of splitting the lens sample into blue and red subsamples, according to the definition from Bell et al. (2004), are shown in the right panel of Fig. 2 and in Table 1. For the color-separated sample (right panel of Fig. 1) we have ignored the (basically uncorrelated) shear contributions from the lenses of the respectively other color-bin; however, we have verified that a simultaneous fit of both sub-samples yields indistinguishable results. The red sample contains only 20% of all lenses by number but yields even tighter constraints than the fourfold larger blue sample. This clearly demonstrates that the galaxy-galaxy lensing signal is dominated by red galaxies. Furthermore, at a given luminosity red galaxies have a larger velocity dispersion than blue galaxies. The best-fit velocity dispersion at $L_\star$ is about 40% larger for red galaxies implying that their (aperture) mass is about twice that of blue galaxies. The scaling η does not differ between the two subsamples.

5. Results from the NFW profile

5.1. Model

The density distribution of the NFW profile (Navarro et al. 1995, 1996, 1997) is given by

$$\rho(r) = \frac{\delta_{\rm c}\,\rho_{\rm c}}{(r/r_{\rm s})(1+r/r_{\rm s})^2}, \tag{8}$$

where $\delta_{\rm c}$ is a characteristic density, $\rho_{\rm c}$ is the critical cosmological density and $r_{\rm s}$ is a scale radius. At $r \sim r_{\rm s}$ the density profile turns from $\rho(r) \propto r^{-1}$ to $\rho(r) \propto r^{-3}$. The virial radius $r_{\rm vir}$ is defined as the radius inside which the mean density is 200 times the mean density of the universe. (NB: this is *not* the same definition of the virial radius as the one based on 200 times the critical density of the universe.) The mass inside the virial radius defines the virial mass

$$M_{\rm vir} = \frac{800}{3}\pi\rho_{\rm m} r_{\rm vir}^3 \tag{9}$$

with $\rho_{\rm m} = \Omega_{\rm m}\rho_c$. The ratio between virial radius und scale radius is the concentration

$$c = r_{\rm vir}/r_{\rm s}. \tag{10}$$

From Eqs. (8)–(10) follows the relation between the characteristic density and the concentration

$$\delta_{\rm c} = \frac{200\,\Omega_{\rm m}}{3}\,\frac{c^3}{\ln(1+c) - c/(1+c)}. \tag{11}$$

In analogy to the Tully-Fisher and Faber-Jackson relations, which imply a relation between luminosity and mass, we impose a similar relation between the virial radius (a proxy for the virial mass) and luminosity here,

$$\frac{r_{\rm vir}}{r^*_{\rm vir}} = \left(\frac{L}{L_*}\right)^\alpha. \tag{12}$$

The virial mass-to-light ratio is thus given by

$$\frac{M_{\rm vir}}{L} = \frac{800}{3}\pi\rho_{\rm m}\frac{r_{\rm vir}^3}{L} \propto L^{3\alpha-1}. \tag{13}$$

A constant mass-to-light ratio $M/L \propto L^0 = $ const. requires $\alpha = 1/3$.

The shear from the NFW model is calculated in Bartelmann (1996) and Wright & Brainerd (2000). Formally, NFW profiles are a two-parameter family, e.g. with $M_{\rm vir}$ and c as possible choices. Yet, for a given cosmological model (e.g. ΛCDM), redshift (e.g. $z \approx 0.5$) and halo mass scale, N-body simulations show that c has only little scatter.

5.2. Constraints on the concentration c

First, we try to constrain the virial radius $r^*_{\rm vir}$ and the concentration c for a fixed α. Figure 3 shows results for the whole lens sample with $\alpha = 0.3$ and $r_{\rm max} = 400h^{-1}$ kpc. Using $\alpha = 0$ instead does not change the shape of the contours but just shifts them toward lower values of $r^*_{\rm vir}$. As Fig. 3 shows, weak lensing provides only poor constraints on c: only a lower bound can be obtained. The 1-σ lower limit for c alone is $c > 29$, the 2-σ lower limit is $c > 11$. In the following, we will use a fixed $c \equiv 20$. This choice is somewhat arbitrary. However, smaller values of c are disfavoured by our data. We checked that assuming a smaller c

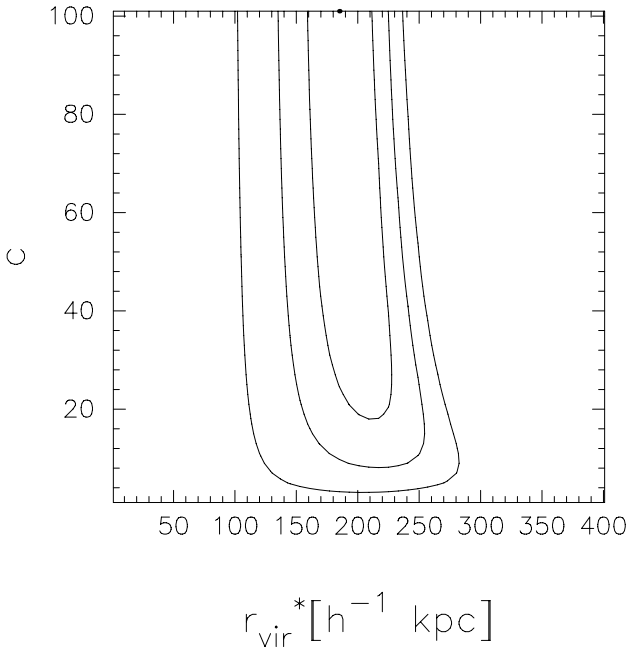

Fig. 3. Constraints on the virial radius $r^*_{\rm vir}$ and the concentration c for the NFW profile obtained from the full lens sample with $\alpha = 0.3$ fixed and $r_{\rm max} = 400h^{-1}$ kpc. The viral radius $r_{\rm vir}$ and the concentration c are defined as detailed in Sect. 5.1.

does not change the best-fit results of our fits but would increase the error bars[1].

5.3. Results for all galaxies

Using all lenses, $c \equiv 20$ and $r_{\rm max} = 400h^{-1}$ kpc we obtain the likelihood contours shown in the left panel of Fig. 4. The best-fit parameters with 1-σ error bars are $r^*_{\rm vir} = 209^{+24}_{-32}h^{-1}$ kpc and $\alpha = 0.34^{+0.12}_{-0.16}$. The corresponding virial mass is $\log(hM^*_{\rm vir}/M_\odot) = 11.8^{+0.1}_{-0.3}$. This mass estimate is considerably smaller than the mass estimate from the SIS model ($M_{\rm SIS}(r \le 150h^{-1}\ {\rm kpc}) = 1.70^{+0.41}_{-0.48} \times 10^{12}h^{-1}\ M_\odot$, see Table 1), although the virial mass even encloses a larger radius than the aperture used for the SIS model. Wright & Brainerd (2000) already pointed out that for galaxy-sized halos the SIS model yields much larger mass estimates than the NFW model. Decreasing $r_{\rm max}$ from $r_{\rm max} = 400h^{-1}$ kpc to $250h^{-1}$ kpc or $150h^{-1}$ kpc yields larger $r^*_{\rm vir}$ and smaller α, $r^*_{\rm vir} = 233^{+24}_{-32}h^{-1}$ kpc and $\alpha = 0.26^{+0.12}_{-0.08}$ for $r_{\rm max} = 150h^{-1}$ kpc. Unlike the SIS model, the differences here are within the 1-σ uncertainties. Therefore, it seems that the NFW profile provides a better fit to the data than the SIS model. However, the tendency to larger virial radii for decreasing $r_{\rm max}$ might indicate that our modelling of NFW profiles also needs refinements.

For the NFW model with $r_{\rm max} = 400h^{-1}$ kpc we obtain a scaling of the virial mass-to-light ratio with luminosity as $M_{\rm vir}/L \propto L^{0.02}$ implying almost the same mass-to-light ratio for all luminosities. In contrast, we find a decreasing mass-to-light ratio at fixed radius with increasing luminosity for the SIS model. However, the scaling relation found from the SIS model is only marginally excluded at the 1-σ level by the measurement from the NFW model.

5.4. Results for blue/red subsamples

Analogously to the SIS case, we split the lens sample into a blue and a red subsample; the results, using $r_{\rm max} = 400h^{-1}$ kpc, are shown in the right panel of Fig. 4 and in Table 2. We find that red galaxies have a larger virial radius at a given luminosity $L_\star$ and a larger α than blue galaxies. However, the significance of these differences is only about 1σ. The larger virial radius for the red galaxies implies a virial mass that is almost a factor of 2 larger than that of equally luminous blue galaxies. Even within the virial radius of the blue $L_\star$ galaxies, the mass of red $L_\star$ galaxies is much larger, $\log(hM^*_{\rm red}(r \le 177h^{-1}\ {\rm kpc})/M_\odot) = 11.8 \pm 0.3$. Formally, the best-fit mass-to-light ratios scale with luminosity as $M_{\rm vir}/L \propto L^{-0.46}$ for blue galaxies and as $M_{\rm vir}/L \propto L^{0.26}$ for red ones, but for both subsamples a mass-to-light ratio independent of luminosity is consistent with the data.

6. Influence of clusters

One of the COMBO-17 fields – the A 901 field – has been chosen specifically to study the supercluster composed of the components Abell 901a, 901b and 902 at a redshift of $z = 0.16$ (Gray et al. 2002, 2004). Later, another cluster (named CBI in Taylor et al. 2004) was detected behind Abell 902 using the 3D distribution of galaxies. The masses of these four clusters were measured jointly using weak lensing (Taylor et al. 2004). Table 3 shows central positions, redshifts and velocity dispersions for the different clusters modelled as SISs. We address in this section the influence of these clusters on our galaxy-galaxy lensing measurements. Two measurements are compared: one ignoring the presence of the clusters and one including the shear from the clusters $\gamma_{\rm cl}$. In the second case, Eq. (2) becomes

$$\epsilon_j^{(s)} = \epsilon_j - \gamma_j - \gamma_{\rm cl}. \qquad (14)$$

The shear of the clusters is computed assuming isothermals spheres (see Eq. (7)) with the parameters from Table 3. The lens galaxies are also modelled as isothermal spheres, see Sect. 4. Instead of using the shear γ of the clusters we also tried using the reduced shear $g = \gamma/(1-\kappa)$ and including the magnification $\mu = ((1-\kappa)^2 - \gamma^2)^{-1}$ to correct the luminosities of the lenses, the convergence κ here, being calculated from the SIS fits of the clusters. We found that the difference to just using γ in both cases is negligible.

The S 11 field contains the cluster Abell 1364 at a redshift $z = 0.11$ for which we fit a velocity dispersion

[1] Note that the value of c is dependent on our definition of the virial radius. Unfortunately, there is no unique definition of the virial radius in the literature. Sometimes it is referred to as the radius inside which the mean density is some over-density times the *mean* density of the universe, and sometimes as the radius inside which the mean density is some over-density times the *critical* density of the universe. Changing the definition of the virial radius would change relation (11) and therefore c. The shape of the density profile remains unaffected so that the values of the scale radius $r_{\rm s}$ and the characteristic density $\delta_{\rm c}$ do not change. Defining the virial radius as the radius inside which the mean density is 200 times the critical density instead of our definition from Sect. 5.1 would lower the concentration from $c = 20$ to approximately $c' = 12.4$. The virial radius would therefore become about $r'_{\rm vir} = 0.62\ r_{\rm vir}$ and the virial mass $M'_{\rm vir} = 0.79\ M_{\rm vir}$. The lower limits on c that we obtained from our data would roughly become $c' > 18$ (1-σ) and $c' > 7$ (2-σ). Our choice of $c \equiv 20$ ($c' = 12.4$) appears somewhat large for galaxy-sized halos (see e.g. Bullock et al. 2001), however, we stress that smaller values of c are disfavoured by our data.
We emphasize the differences in the definition of the virial radius here only for clarity and easier comparability to other works. All figures and results presented in this paper use the definition of the virial radius given in Sect. 5.1.

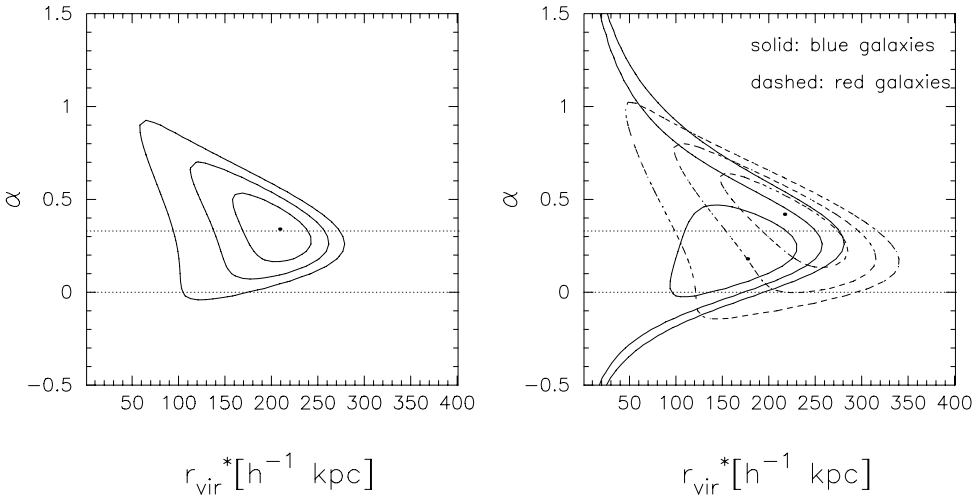

Fig. 4. Constraints on the virial radius $r^*_{\rm vir}$ and its scaling with luminosity (α) inside $r_{\rm max} = 400h^{-1}$ kpc for the NFW profile using all lenses (*left panel*) and subsamples of blue and red lenses (*right panel*). Contours are 1-, 2- and 3-σ.

Table 2. Constraints on dark matter halos of galaxies modelled by NFW profiles for different lens samples and $r_{\rm max} = 400h^{-1}$ kpc. $N_{\rm d}$, $N_{\rm s}$ and $N_{\rm p}$ are the numbers of lenses, sources and pairs in each measurement. These numbers differ from those given in Table 1 because of the larger $r_{\rm max}$ used here. The virial radius $r^*_{\rm vir}$ and α are fitted quantities (see Fig. 4), the virial mass $M^*_{\rm vir}$ and the virial mass-to-light ratio $M^*_{\rm vir}/L^*$ are calculated from $r^*_{\rm vir}$. $\beta = 3\alpha - 1$ gives the scaling of $M_{\rm vir}/L$ with luminosity, $M_{\rm vir}/L \propto L^\beta$. All errors are 1-$\sigma$.

Lenses	$N_{\rm d}$	$N_{\rm s}$	$N_{\rm p}$	$r^*_{\rm vir}$ [h^{-1} kpc]	α	$\log(h\frac{M_{\rm vir}}{M_\odot})$	$M^*_{\rm vir}/L^*$ [$h(M/L)_\odot$]	β
all	11 311	13 956	566 466	209^{+24}_{-32}	$0.34^{+0.12}_{-0.16}$	$11.8^{+0.1}_{-0.3}$	64^{+25}_{-33}	$0.02^{+0.36}_{-0.48}$
blue	9181	13 936	451 420	177^{+40}_{-48}	$0.18^{+0.20}_{-0.12}$	$11.6^{+0.3}_{-0.4}$	39^{+33}_{-24}	$-0.46^{+0.60}_{-0.36}$
red	2130	13 603	115 046	217^{+56}_{-48}	$0.42^{+0.16}_{-0.20}$	$11.9^{+0.3}_{-0.3}$	71^{+71}_{-38}	$0.26^{+0.48}_{-0.60}$

Table 3. Central positions, redshifts and velocity dispersions of the known clusters in the A 901 field (Taylor et al. 2004).

	$\alpha_{\rm J2000}$	$\delta_{\rm J2000}$	z	σ_v [km s^{-1}]
A901a	$09^{\rm h}56^{\rm m}26.4^{\rm s}$	$-09^{\rm h}57^{\rm m}21.7^{\rm s}$	0.16	680^{+25}_{-90}
A901b	$09^{\rm h}55^{\rm m}57.4^{\rm s}$	$-09^{\rm h}59^{\rm m}02.7^{\rm s}$	0.16	600^{+40}_{-85}
A902	$09^{\rm h}56^{\rm m}33.6^{\rm s}$	$-10^{\rm h}09^{\rm m}13.1^{\rm s}$	0.16	470^{+100}_{-280}
CBI	$09^{\rm h}56^{\rm m}39.6^{\rm s}$	$-10^{\rm h}10^{\rm m}21.6^{\rm s}$	0.48	730^{+160}_{-340}

$\sigma = 615^{+110}_{-140}$ km s^{-1}. As for the foreground clusters in the A 901 field, we compare measurements for the S 11 field, first including and then ignoring the cluster shear. We find that the cluster shear is negligible for the S 11 field.

6.1. Influence of foreground clusters at z = 0.16

Because only lens galaxies with $0.2 < z_{\rm d} < 0.7$ have been considered, the lens sample should contain no galaxies that lie in the foreground clusters (Abell 901a/b, Abell 902). The expectation is that the foreground clusters will not influence the galaxy-galaxy lensing measurements because the shear from the foreground clusters will be in random directions with respect to the orientations of the lens-source pairs used for galaxy-galaxy lensing.

The left panel of Fig. 5 shows likelihood contours obtained from the A 901 field both ignoring and including the shear from the foreground clusters Abell 901a/b and Abell 902. The shear from CBI is ignored. Hardly any difference is seen between both cases, from which we measure $\sigma_\star = 174^{+24}_{-24}$ km s^{-1} and $\eta = 0.34^{+0.12}_{-0.09}$ (1-σ errors).

As a second test we ignore the cluster shear but exclude all sources from the galaxy-galaxy lensing measurement for which the convergence κ (and thus the shear γ) from the foreground clusters exceeds some threshold. Figure 6 shows that from the foreground clusters alone $\kappa < 0.1$ for almost all sources. The maximum is $\kappa = 0.17$. Therefore the weak shear limit is still valid in Eq. (14). When excluding all sources with $\kappa > 0.05$ (224 out of 6481 sources), the difference to the measurement using all sources is negligible. When excluding further sources, the contours start to widen significantly but maintain the same minimum. This widening can be explained by the decreasing number statistics. In particular, we do not see any hint of a bias from the clusters. When excluding the 22% of sources with $\kappa > 0.025$, the 3-σ contour remains closed. The best-fit parameters with 1-σ errors are then $\sigma_\star = 180^{+24}_{-30}$ km s^{-1} and $\eta = 0.31 \pm 0.12$.

6.2. Influence of CBI at z = 0.48

The cluster CBI has a redshift $z = 0.48$ and therefore some of the lens galaxies will reside in the cluster halo. This implies that additional mass is present around these galaxies. Ignoring the cluster CBI, this additional mass will be assigned to the galaxies and thus the derived masses (or velocity dispersions) will be too high. Guzik & Seljak (2002) modelled this case for the SDSS data. They find from theoretical models that clusters increase the shear measurements of galaxies. The strength of this effect depends on the distance from the lens center, it increases from zero

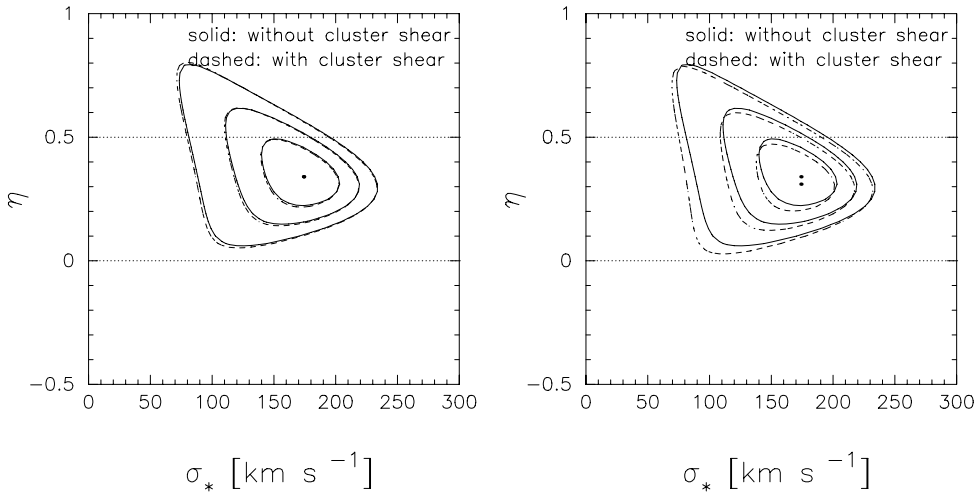

Fig. 5. Influence of the clusters shear on the galaxy-galaxy lensing measurement. Solid lines refer to measurements ignoring the cluster shear, dashed lines to measurements including the cluster shear. In the left panel, only the foreground clusters Abell 901a/b and Abell 902 are taken into account. In the right panel also the background cluster CBI is used. A maximum projected separation between lenses and sources of $r_{\rm max} = 150h^{-1}$ kpc is used.

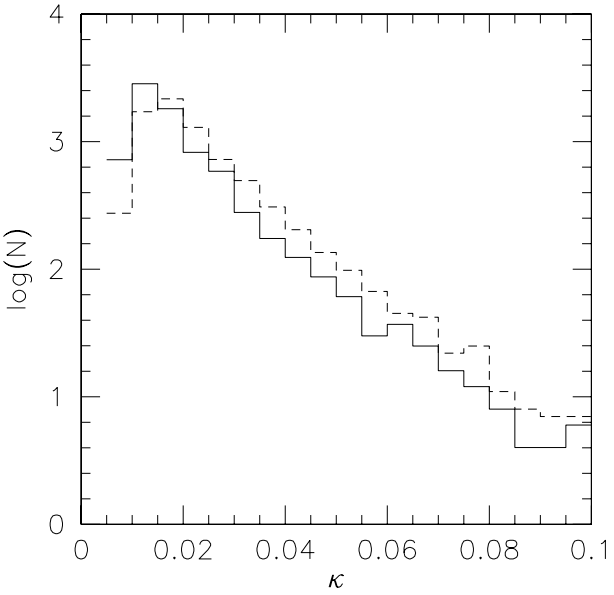

Fig. 6. Histogram over κ due to the foreground clusters only (solid) and due to the foreground clusters and CBI together (dashed).

toward a maximum around $r = 200h^{-1}$ kpc and then decreases again. The peak contribution and the shape of the decrease depend on the details of the model.

The right panel of Fig. 5 shows the same as the left panel but this time includes the shear from CBI in the cluster measurement. Although the change in the contours is clearly visible, the shear from the background cluster CBI does not seem to have a big influence; the contours only widen marginally. The best-fit parameters with their 1-σ errors become $\sigma_\star = 174^{+24}_{-24}$ km s^{-1} and $\eta = 0.31^{+0.12}_{-0.09}$. Note, however, that the resolution of our grid in parameter space is only $\Delta\eta = 0.03$.

As a second test we again ignore the cluster shear and exclude objects with large κ from both the foreground clusters and CBI. Figure 6 shows a histogram of κ, the maximum of which is $\kappa = 0.26$. When excluding all sources with $\kappa > 0.05$ we obtain likelihood contours similar to the case when including the cluster shear. 345 out of 6481 sources are then excluded. Excluding further sources results in wider contours. The 3-σ contour stays closed when we exclude sources with $\kappa > 0.03$. These are 22% of all sources and the contours do not shift compared to the case where the cluster shear is ignored.

A third test is to exclude all lenses that are close to the center of the background cluster CBI. We exclude every lens lying within $1h^{-1}$ Mpc projected separation from the cluster center (corresponding to $\theta = 240''$ angular separation) and with a redshift difference less than 0.2. These are 221 out of 4444 lenses. The likelihood contours hardly change when these lenses are excluded.

From all these tests we conclude that our results are not biased from the presence of several clusters in the A 901 field. This conclusion also holds when the SIS model is fitted within $r_{\rm max} = 400h^{-1}$ kpc instead of $150h^{-1}$ kpc. The little influence even the background cluster CBI has might be surprising but it is understandable given the small number of lenses that actually reside within this cluster. In particular we note that the comparably large value of $\sigma_\star$ obtained from the A 901 field which is about 1-σ higher than from all three fields together is not caused directly by the clusters. Instead, it seems that cosmic variance is still an issue even on the scales of our survey fields.

7. Comparison to other surveys

In this section, we compare our results to those from previous galaxy-galaxy lensing studies. Any such comparison is limited by the very different data sets and techniques used in the different investigations. For our comparison, we concentrate on results from the RCS (Hoekstra et al. 2004) and the SDSS (Guzik & Seljak 2002; Seljak et al. 2005) data.

7.1. Comparison to the RCS

The galaxy-galaxy lensing analysis from the RCS (Hoekstra et al. 2004) is in many regards similar to the one presented here and thus very suitable for a comparison of results. Both surveys reach a comparable depth so that one can expect that comparable sets of lens galaxies are probed. Further,

Hoekstra et al. (2004) use the maximum-likelihood technique by Schneider & Rix (1997), model lenses as SISs and by NFW profiles and fit to a fiducial lens galaxy with a characteristic luminosity $L_\star$, just as we do. Note, in particular, that Hoekstra et al. (2004) use the same definition of the virial radius of the NFW profile as we do (see Sect. 5.1).

However, crucial differences exist. The area of the RCS used for the galaxy-galaxy lensing analysis is 45.5 deg^2, so about 60 times larger than that used here. On the other hand, Hoekstra et al. (2004) only have observations in a single filter available. Therefore, they have to select lenses and sources based on magnitude cuts and they have to use redshift probability distributions for estimating luminosities and for shear calibration. Furthermore, Hoekstra et al. (2004) can only investigate lens galaxy halos on an angular scale while we are able to probe the same physical scale of all lenses. Third, there is no easy way to implement halo scalings with luminosity, nor to separate lenses by their rest-frame color. Hoekstra et al. (2004) fit their models within 2′ which they estimate corresponds to about $350h^{-1}$ kpc at the mean redshift of the lenses. This is considerably larger than the region we probe for the SIS model ($r_{\rm max} = 150h^{-1}$ kpc) and comparable to the region probed for the NFW profile ($r_{\rm max} = 400h^{-1}$ kpc). Another difference lies in the definition of the fiducial luminosity. We use $L_\star = 10^{10}h^{-2}\,L_{r,\odot}$ measured in the SDSS r-band while Hoekstra et al. (2004) use $L_B = 10^{10}h^{-2}\,L_{B,\odot}$ as reference. From our data set we calculate that lenses with $L_B = 10^{10}h^{-2}\,L_{B,\odot}$ have SDSS-r-band luminosities of about $L_r = 1.1 \times 10^{10}h^{-2}\,L_{r,\odot}$. In Kleinheinrich et al. (2005) it is shown for the SIS that it is not possible to constrain the scaling relation between velocity dispersion and luminosity without multi-color data. Therefore, Hoekstra et al. (2004) have to assume this scaling relation unlike being able to fit it as we do.

7.1.1. SIS model

For better comparability with the RCS results we redo our fit to the SIS model with $L_\star = 1.1 \times 10^{10}h^{-2}\,L_{r,\odot}$ and $r_{\rm max} = 350h^{-1}$ kpc. We obtain $\sigma_\star = 132^{+18}_{-24}$ km s^{-1} and $\eta = 0.37^{+0.15}_{-0.15}$ from the whole lens sample.

Hoekstra et al. (2004) do not specifically fit the SIS model using the maximum-likelihood technique of Schneider & Rix (1997). Instead, they fit the SIS model to the measured galaxy-mass cross-correlation, and they constrain the truncated SIS model using the maximum-likelihood technique. The velocity dispersion obtained from the truncated SIS model becomes that of the SIS in the limit of infinite truncation parameter s. In both cases, Hoekstra et al. (2004) assume a scaling relation as in Eq. (5) with $\eta = 0.3$ and a characteristic luminosity $L_\star$ as detailed in Sect. 7.1. From the galaxy-mass cross-correlation function they obtain $\sigma_\star = 140 \pm 4 \pm 3$ km s^{-1}. The truncated SIS yields $\sigma_\star = 136 \pm 5 \pm 3$ km s^{-1}. Both results are in good agreement with our results. Conversely, we are able to confirm the value of η adopted by Hoekstra et al. (2004).

The error bars of Hoekstra et al. (2004) are about 5 times smaller than ours. From the difference in area between the RCS and COMBO-17 one would even expect a factor of about $\sqrt{60} \approx 8$ difference. That their error bars are not that much smaller can be attributed to the detailed classification and redshifts available in COMBO-17. In Kleinheinrich et al. (2005) it is shown that the error bar on $\sigma_\star$ increases by about 30% when redshifts are omitted. The influence of accurate redshift estimates on the determination of η is found to be much more severe – from just a single passband no meaningful constraints on η can be derived. This explains why we are able to fit η while Hoekstra et al. (2004) had to assume a fixed value.

7.1.2. NFW profile

For better comparability with the RCS we also redo our fit to the NFW profile with $L_\star = 1.1{\times}10^{10}h^{-2}\,L_{r,\odot}$ and $r_{\rm max} = 350h^{-1}$ kpc. We obtain $r^*_{\rm vir} = 217^{+24}_{-32}h^{-1}$ kpc and $\alpha = 0.30^{+0.16}_{-0.12}$ from the whole lens sample. This corresponds to a virial mass $\log(hM^*_{\rm vir}/M_\odot) = 11.9^{+0.1}_{-0.2}$.

The exact modelling of Hoekstra et al. (2004) is somewhat different from ours. While we fit the virial radius and its scaling with luminosity, Hoekstra et al. (2004) assume scaling relations between the maximum rotation velocity and virial mass, respectively, with luminosity and fit the virial velocity $v_{\rm vir}$ and the scale radius r_s. The virial velocity is directly related to the virial mass and virial radius by $v_{\rm vir} = \sqrt{GM_{\rm vir}/r_{\rm vir}} \propto r_{\rm vir}$. All three quantities are independent of the scale radius r_s. Therefore, we can readily compare our results on the virial mass to those from Hoekstra et al. (2004). They find $\log(hM^*_{\rm vir}/M_\odot) = 11.9 \pm 0.1$ in good agreement with our result. Furthermore, their constraint on the scale radius $r_{\rm s} = 16.2^{+3.6}_{-2.9}h^{-1}$ kpc is roughly consistent with the scale radius implied by the virial radius we find and the concentration we assume.

7.2. Comparison to the SDSS

While COMBO-17 and the RCS are both deep surveys from which lens galaxies at redshifts $z_{\rm d} \approx 0.4$ can be probed, the SDSS is a much shallower survey with a correspondingly small average lens redshift. To date, several observational weak lensing analyses have been published investigating different aspects of dark matter halos of galaxies and using consecutively larger parts of the survey (Fischer et al. 2000; McKay et al. 2001; Seljak 2002; Guzik & Seljak 2002; Sheldon et al. 2004; Seljak et al. 2005). For the comparison to our results we will concentrate on the results by Guzik & Seljak (2002).

Guzik & Seljak (2002) use the halo model for their galaxy-galaxy lensing analysis. This model takes not only the contribution from galaxies themselves into account but also from the surrounding group and cluster halos. This of course complicates the comparison. On the other hand, Guzik & Seljak (2002) find that on average only about 20% of the galaxies are non-central galaxies, for which the group/cluster contribution is important. Therefore, the group/cluster contribution to our mass estimates is probably well within our error bars. Guzik & Seljak (2002) only fit NFW profiles to their data. They define the virial radius as radius inside which the mean density is 200 times the critical density of the universe. Therefore, we have to multiply our virial masses by a factor 0.79 to compare them to theirs. Similar to our approach, Guzik & Seljak (2002) assume a relation between mass and luminosity $M/M_\star = (L/L_\star)^\beta$. $M_\star$ and β are derived from different passbands. Here, we just compare to the results from the r'-band in which the reference luminosity is $L_\star = 1.51 \times 10^{10}h^{-2}\,L_\odot$.

7.2.1. All galaxies

Assuming that group/cluster halos only contribute to the faintest lens galaxies, Guzik & Seljak (2002) find a virial mass $\log(hM'^*_{\rm vir}/M_\odot) = 12.0 \pm 0.1$. and $\beta = 1.51 \pm 0.16$. Our measurement of $r^*_{\rm vir}$ implies for a galaxy with $L = 1.5 \times 10^{10}h^{-2}\,L_{r,\odot}$

a virial radius of $r_{\rm vir} = 240^{+27}_{-37} h^{-1}$ kpc. Here, we have used the measured $\alpha = 0.34$ and ignored its errors and still use our definition of the virial radius. Changing to the definition adopted by Guzik & Seljak (2002) this corresponds to a virial mass of $\log(hM'^{*}_{\rm vir}/M_\odot) = 11.9^{+0.1}_{-0.2}$ in very good agreement with the result from the SDSS. Our measurement of $\alpha = 0.34^{+0.12}_{-0.16}$ corresponds to $\beta = 1.02^{+0.36}_{-0.48}$. This is smaller than the value found by Guzik & Seljak (2002) but the difference is not very significant. When Guzik & Seljak (2002) assume the same group/cluster contribution for all luminosity bins, their best-fit β drops to $\beta = 1.34 \pm 0.17$. Therefore it might well be that the differences between COMBO-17 and the SDSS concerning the scaling between mass and light is due to the differences in the modelling.

7.2.2. Early-/late-type subsamples

Guzik & Seljak (2002) also split the lens sample into early- and late-type subsamples. Both samples contain about equal numbers. This already indicates that these subsamples cannot be too similar to our subsamples of red and blue galaxies in which only about 20% of all galaxies belong to the red subsample. However, we should at least be able to see similar trends from late-type to early-type galaxies as from blue to red ones. Guzik & Seljak (2002) fix the scaling of the mass with luminosity to the value derived for the whole lens sample ($\beta = 1.51$) and also adopt the same $L_\star = 1.51 \times 10^{10} h^{-2}\ L_\odot$ for both subsamples. For late-type galaxies they find a virial mass of $L_\star$-galaxies of $\log(hM'^{*}_{\rm vir}/M_\odot) = 11.5^{+0.2}_{-0.4}$, for early-type galaxies they find $\log(hM'^{*}_{\rm vir}/M_\odot) = 12.0 \pm 0.1$, We scale the virial radii of blue and red galaxies measured at $L = 10^{10} h^{-2}\ L_\odot$ to the higher $L_\star$ used by Guzik & Seljak (2002) using the measured α for the two samples and calculate from that the virial masses assuming the same definition as Guzik & Seljak (2002). We obtain $\log(hM'^{*}_{\rm vir}/M_\odot) = 11.6^{+0.3}_{-0.4}$ for the blue sample and $\log(hM'^{*}_{\rm vir}/M_\odot) = 12.0 \pm 0.3$ for the red sample. The agreement with the SDSS results is surprisingly good given the different definitions of the subsamples and the different lens redshifts. Most importantly, from both surveys we see the same trend that early-type or red galaxies have 2−3 times more massive halos than late-type or blue galaxies at the same luminosity.

8. Summary

We have presented a galaxy-galaxy lensing analysis of three fields from the COMBO-17 survey. Despite the limited area, the data set is unique at intermediate redshift in its extensive redshift information that allows us to separate the 12 000 lens galaxies according to their physical properties such as luminosity and rest-frame colors. Although one of these fields is centered on a foreground supercluster, we have shown that our measurements are not biased from the presence of the supercluster. In addition, a cluster at $z = 0.48$ behind the supercluster was also found to have remarkably little influence.

Using a model to link lens galaxies to their dark matter halos, either SIS or NFW, we constrained the halo parameters through galaxy-galaxy lensing. For both halo models, we find that, at the same luminosity $L_\star = 10^{10} h^{-2}\ L_\odot$, red galaxies have dark matter halos about twice as massive as blue ones. For SIS models within $150 h^{-1}$ kpc we obtain $\log(hM_\star/M_\odot) = 12.0^{+0.2}_{-0.3}$ for blue galaxies and $\log(hM_\star/M_\odot) = 12.4^{+0.1}_{-0.2}$ for red galaxies. Adopting NFW profiles we find virial masses $\log(hM^{*}_{\rm vir}/M_\odot) = 11.6^{+0.3}_{-0.4}$ for blue galaxies and $\log(hM^{*}_{\rm vir}/M_\odot) = 11.9 \pm 0.3$ for red galaxies. Note that the virial masses are defined as masses inside a sphere with mean density equal to 200 times the mean density of the universe. For $M^{*}_{\rm vir} = 5 \times 10^{11} h^{-1}\ M_\odot$ this is about $200 h^{-1}$ kpc. Changing this definition to the mass inside a sphere with mean density equal to 200 times the critical density of the universe would lower the virial masses by about 20%. The mass estimates from the SIS model are considerably larger than from the NFW profile although the virial radii exceed the aperture adopted for the mass estimate of the SISs. However, it has been shown by Wright & Brainerd (2000) that such behaviour is expected.

For both models, we also fit the scaling between mass and luminosity. In the SIS model we find approximately the same scaling for blue and red galaxies, about $M \propto L^{0.5}$ inside $150 h^{-1}$ kpc. For the NFW model we find a similar scaling relation for blue galaxies, but $M_{\rm vir} \propto L^{1.26}$ for red galaxies. The differences between the two models and between the two subsamples for the NFW model may arise from the different scales over which the fitted mass-luminosity relation applies. For the SIS model it is always fitted over a fixed aperture of $150 h^{-1}$ kpc while for the NFW profile it only applies to the mass within the virial radius that differs between blue and red galaxies.

Finally, we compared our results to those obtained from the RCS and the SDSS. We pointed out that for such a comparison it is indispensable to compare results from similar modellings. As far as possible we translated our measurements to the modelling approaches of Hoekstra et al. (2004) for the RCS and Guzik & Seljak (2002) for the SDSS and found consistent results. We deem this remarkable, at least because the modelling of Guzik & Seljak (2002) is very different from ours. A more exact comparison between COMBO-17 and the SDSS adopting the same techniques is beyond the scope of this paper, although such an investigation would be very valuable. The fact that both surveys probe galaxies in different redshift ranges would in principle allow a measurement of the evolution of dark matter halos.

Acknowledgements. We thank the anonymous referee for helpful suggestions. C.W. was supported by a PPARC Advanced Fellowship. M.K. acknowledges support by the BMBF/DLR (project 50 OR 0106)), by the DFG under the project SCHN 342/3–1, and by the DFG-SFB 439.

References

Bartelmann, M. 1996, A&A, 313, 697
Bell, E. F., Wolf, C., Meisenheimer, K., et al. 2004, ApJ, 608, 752
Brainerd, T. G. 2004, in The New Cosmology: Conference on Strings and Cosmology, ed. R. E. Allen, D. V. Nanopoulos, & C. N. Pope, AIP Conf. Proc., 743, 129
Brainerd, T. G., & Specian, M. A. 2003, ApJ, 593, L7
Brainerd, T. G., Blandford, R. D., & Smail, I. 1996, ApJ, 466, 623
Bullock, J. S., Kolatt, T. S., Sigad, Y., et al. 2001, MNRAS, 321, 559
Conroy, C., Newman, J. A., Davis, M., et al. 2005, ApJ, 635, 982
Danziger, I. J. 1997, in Dark and Visible Matter in Galaxies and Cosmological Implications, ASP Conf. Ser., 117, 28
dell'Antonio, I. P., & Tyson, J. A. 1996, ApJ, 473, L17
Erben, T., Van Waerbeke, L., Bertin, E., Mellier, Y., & Schneider, P. 2001, A&A, 366, 717
Fischer, P., McKay, T. A., Sheldon, E., et al. 2000, AJ, 120, 1198
Gray, M. E., Taylor, A. N., Meisenheimer, K., et al. 2002, ApJ, 568, 141
Gray, M. E., Wolf, C., Meisenheimer, K., et al. 2004, MNRAS, 347, L73
Griffiths, R. E., Casertano, S., Im, M., & Ratnatunga, K. U. 1996, MNRAS, 282, 1159
Guzik, J., & Seljak, U. 2002, MNRAS, 335, 311
Heymans, C., & Heavens, A. 2003, MNRAS, 339, 711
Hoekstra, H., Franx, M., & Kuijken, K. 2000, ApJ, 532, 88
Hoekstra, H., Franx, M., Kuijken, K., Carlberg, R. G., & Yee, H. K. C. 2003, MNRAS, 340, 609
Hoekstra, H., Yee, H. K. C., & Gladders, M. D. 2004, ApJ, 606, 67
Hudson, M. J., Gwyn, S. D. J., Dahle, H., & Kaiser, N. 1998, ApJ, 503, 531
Kaiser, N., Squires, G., & Broadhurst, T. 1995, ApJ, 449, 460
King, L., & Schneider, P. 2002, A&A, 396, 411
Kleinheinrich, M., Rix, H.-W., Erben, T., et al. 2005, A&A, 439, 513

Kochanek, C. S., Schneider, P., & Wambsganss, J. 2004, Gravitational Lensing: Strong, Weak & Micro, Proceedings of the 33rd Saas-Fee Advanced Course, ed. G. Meylan, P. Jetzer & P. North (Berlin: Springer-Verlag)
Le Fèvre, O., Vettolani, G., Garilli, B., et al. 2005, A&A, 439, 845
Luppino, G. A., & Kaiser, N. 1997, ApJ, 475, 20
McKay, T. A., Sheldon, E. S., Racusin, J., et al. 2001, [arXiv:astro-ph/0108013]
McKay, T. A., Sheldon, E. S., Johnston, D., et al. 2002, ApJ, 571, L85
Navarro, J. F., Frenk, C. S., & White, S. D. M. 1995, MNRAS, 275, 720
Navarro, J. F., Frenk, C. S., & White, S. D. M. 1996, ApJ, 462, 563
Navarro, J. F., Frenk, C. S., & White, S. D. M. 1997, ApJ, 490, 493
Prada, F., Vitvitska, M., Klypin, A., et al. 2003, ApJ, 598, 260
Rix, H., de Zeeuw, P. T., Cretton, N., van der Marel, R. P., & Carollo, C. M. 1997, ApJ, 488, 702
Schirmer, M., Erben, T., Schneider, P., et al. 2003, A&A, 407, 869
Schneider, P., & Rix, H. 1997, ApJ, 474, 25
Seljak, U. 2002, MNRAS, 334, 797
Seljak, U., Makarov, A., Mandelbaum, R., et al. 2005, Phys. Rev. D, 71, 043511
Sheldon, E. S., Johnston, D. E., Frieman, J. A., et al. 2004, AJ, 127, 2544
Smith, D. R., Bernstein, G. M., Fischer, P., & Jarvis, M. 2001, ApJ, 551, 643
Sofue, Y., & Rubin, V. 2001, ARA&A, 39, 137
Taylor, A. N., Bacon, D. J., Gray, M. E., et al. 2004, MNRAS, 353, 1176
van den Bosch, F. C., Norberg, P., Mo, H. J., & Yang, X. 2004, MNRAS, 352, 1302
Wilson, G., Kaiser, N., Luppino, G. A., & Cowie, L. L. 2001, ApJ, 555, 572
Wolf, C., Dye, S., Kleinheinrich, M., et al. 2001, A&A, 377, 442
Wolf, C., Meisenheimer, K., Rix, H.-W., et al. 2003, A&A, 401, 73
Wolf, C., Meisenheimer, K., Kleinheinrich, M., et al. 2004, A&A, 421, 913
Wright, C. O., & Brainerd, T. G. 2000, ApJ, 534, 34
Zaritsky, D., & White, S. D. M. 1994, ApJ, 435, 599
Zaritsky, D., Smith, R., Frenk, C., & White, S. D. M. 1993, ApJ, 405, 464
Zaritsky, D., Smith, R., Frenk, C., & White, S. D. M. 1997, ApJ, 478, 39